SIMULATING PROTOSTELLAR JETS SIMULTANEOUSLY AT LAUNCHING AND OBSERVATIONAL SCALES

Jon P. Ramsey and David A. Clarke
Institute for Computational Astrophysics, Department of Astronomy & Physics, Saint Mary's University, Halifax, Nova Scotia B3H 3C3, Canada

ABSTRACT

We present the first 2.5-dimensional magnetohydrodynamic (MHD) simulations of protostellar jets that include both the region in which the jet is launched magnetocentrifugally at scale lengths <0.1 AU and where the propagating jet is observed at scale lengths $>10^3$ AU. These simulations, performed with the new adaptive mesh refinement MHD code AZEuS, reveal interesting relationships between conditions at the disk surface, such as the magnetic field strength, and direct observables such as proper motion, jet rotation, jet radius, and mass flux. By comparing these quantities with observed values, we present direct numerical evidence that the magnetocentrifugal launching mechanism is capable, by itself, of launching realistic protostellar jets.

Key words: ISM: jets and outflows – magnetohydrodynamics (MHD) – stars: formation

1. INTRODUCTION

Jets and outflows from protostellar objects are fundamental aspects of the current star formation paradigm, and are observed anywhere star formation is ongoing. The mechanism proposed by Blandford & Payne (1982), in which jets are launched from accretion disks by gravitational, magnetic, and centrifugal forces, has been extensively studied numerically (e.g., Uchida & Shibata 1985; Meier et al. 1997; Ouyed & Pudritz 1997a, 1997b, 1999; Krasnopolsky et al. 1999; Vitorino et al. 2002; von Rekowski et al. 2003; Ouyed et al. 2003; Porth & Fendt 2010; Staff et al. 2010). By treating the accretion disk as a boundary condition (e.g., Ustyugova et al. 1995), one can study jet dynamics independently of the disk (e.g., Pudritz et al. 2007) though, in order to resolve the launching mechanism, numerical simulations have not followed the jet beyond 100 AU (e.g., Anderson et al. 2005).

In stark contrast, protostellar jets are $\gtrsim 10^4$ AU long (Bally et al. 2007) and only recently have observations reached within 100 AU of the source (e.g., Hartigan et al. 2004; Coffey et al. 2008). This large-scale difference between observations and simulations makes direct comparisons difficult and, in this work, we aim to close this gap. We present axisymmetric (2.5-dimensional) simulations of protostellar jets launched from the inner AU of a Keplerian disk and follow the jet well into the observational domain (2500 AU). These calculations allow us to address the efficacy of the magnetocentrifugal mechanism and to relate conditions near the disk with directly observable properties of the jet.

The simulations presented herein are performed with an adaptive mesh refinement (AMR) version of *ZEUS-3D* (Clarke 1996, 2010) called AZEuS (Adaptive Zone Eulerian Scheme). The *ZEUS-3D* family of codes is among the best tested, documented, and most widely used astrophysical magnetohydrodynamic (MHD) codes available, though this is the first attempt to couple *ZEUS-3D* with AMR.[1] We have implemented the block-based method of AMR detailed in Berger & Colella (1989) and Bell et al. (1994). Significant effort was spent minimizing errors caused by passing waves across grid boundaries, which is of particular importance to this work. A full description of the code and the changes required for AMR on a fully staggered

mesh will appear in J. P. Ramsey & D. A. Clarke (2011, in preparation).

2. INITIALIZATION

Observationally, the inner radius of a protostellar accretion disk, r_i, is between 3 and 5 R_* (Calvet et al. 2000) and, for a typical T Tauri star ($M = 0.5$ $M_\odot$, $R_* = 2.5$ $R_\odot$), $r_i = 0.05$ AU. Thus, following Ouyed & Pudritz (1997a), we initialize a hydrostatic, force-free atmosphere surrounding a 0.5 $M_\odot$ protostar coupled to a rotating disk with $r_i = 0.05$ AU. However, unlike Ouyed & Pudritz we use an adiabatic equation of state that conserves energy across shocks rather than an isentropic polytropic equation of state, as the distinction becomes important for supermagnetosonic flow (Ouyed et al. 2003).

We solve the equations of ideal MHD[2] ($\gamma = 5/3$) over a total domain of 4096 AU $\times$ 256 AU. To span the desired length scales, nine nested, static grids (refinement ratio 2) are initialized each with an aspect ratio of 4:1 (16:1 for the coarsest grid only) and bottom left corner at the origin. Our finest grid has a domain 4 AU $\times$ 1 AU and a resolution $\Delta z = r_i/8 = 0.00625$ AU which we find sufficient to resolve the launching mechanism. Thus, the effective resolution for the entire domain is >26 billion zones. The simulation highlighted in Section 3 was run to $t = 100$ yr with an average time step in the finest grid of ~ 3 minutes and thus ~ 18 million time steps.

During the simulations, a thin region of low velocity and high poloidal magnetic field, $B_p = \sqrt{B_z^2 + B_r^2}$, develops along the symmetry axis, the edge of which is defined by a large gradient in the toroidal magnetic field, $\partial_r B_\varphi$. Insufficient resolution of $\partial_r B_\varphi$ can lead to numerical instabilities, and grids are added dynamically whenever this gradient is resolved by fewer than five zones.

2.1. The Atmosphere

The atmosphere is initialized in hydrostatic equilibrium (HSE; $v_z = v_r = v_\varphi = 0$). Because the left-hand side of the equation governing HSE,

$$\nabla p + \rho \nabla \phi = 0, \quad (1)$$

---

[1] *ENZO*, a hybrid *N*-body Eulerian code (O'Shea et al. 2004), links AMR with the *hydrodynamical* portion of *ZEUS-2D*.

[2] AZEuS solves either the total or the internal energy equation. We chose the latter because positive-definite pressures trump strict conservation of energy in these simulations; see Clarke (2010).

is not a perfect gradient, differencing it directly on a staggered-mesh can commit sufficient truncation error to render the atmosphere numerically unstable. Thus, we replace $\nabla\phi$ with the corresponding poloidal gravitational acceleration vector,

$$\vec{g} = -\frac{1}{\rho_{\rm h}}\nabla p_{\rm h}, \qquad (2)$$

where $\rho_{\rm h}$ and $p_{\rm h}$ are the hydrostatic density and pressure given by

$$\rho_{\rm h} = \rho_{\rm i}\left(\frac{r_{\rm i}}{\sqrt{r^2+z^2}}\right)^{\frac{1}{\gamma-1}} \quad {\rm and} \quad p_{\rm h} = \frac{p_{\rm i}}{\gamma}\left(\frac{\rho_{\rm h}}{\rho_{\rm i}}\right)^{\gamma}. \qquad (3)$$

Here, $\rho_{\rm i}$ and $p_{\rm i}$ are the initial density and pressure at $r_{\rm i}$ and $p \propto \rho^{\gamma}$ is assumed throughout the atmosphere at $t = 0$. In this way, differencing Equation (1) maintains HSE to within machine round-off error indefinitely.

However, Equations (3) as given are singular at the origin where truncation errors are significant regardless of resolution. These errors can launch a supersonic, narrow jet from the origin destroying the integrity of the simulation. To overcome this problem, we replace the point mass at the origin with a uniform sphere of the same mass and a radius R_0, thus modifying the first of Equations (3) to

$$\left(\frac{\rho_{\rm h}}{\rho_{\rm i}}\right)^{\gamma-1} = \begin{cases} \dfrac{r_{\rm i}}{\sqrt{r^2+z^2}}, & r^2+z^2 \geqslant R_0{}^2; \\[2ex] \dfrac{r_{\rm i}}{R_0}\dfrac{3R_0{}^2-r^2-z^2}{2R_0{}^2}, & r^2+z^2 < R_0{}^2. \end{cases} \qquad (4)$$

If R_0 is sufficiently resolved (e.g., four zones), the numerical jet is eliminated. The resulting "smoothed potential" is superior to a "softened potential" since the former has no measurable effects beyond R_0. Here, we use $R_0 = r_{\rm i}$.

The atmosphere is initialized with the force-free magnetic field used by Ouyed & Pudritz (1997a):

$$A_{\varphi} = \frac{B_{\rm i}}{\sqrt{2-\sqrt{2}}}\frac{\sqrt{r^2+(z+z_{\rm d})^2}-(z+z_{\rm d})}{r};$$

$$B_z = \frac{1}{r}\frac{\partial(rA_{\varphi})}{\partial r}, \qquad B_r = -\frac{\partial A_{\varphi}}{\partial z}, \qquad B_{\varphi} = 0, \qquad (5)$$

where A_{φ} is the vector potential, $z_{\rm d}$ is the disk thickness (set to $r_{\rm i}$), and $B_{\rm i}$ is the magnetic field strength at $r_{\rm i}$, given by

$$B_{\rm i} = \sqrt{\frac{8\pi p_{\rm i}}{\beta_{\rm i}}}. \qquad (6)$$

Here, $p_{\rm i}$ and $\beta_{\rm i}$ (plasma beta at $r_{\rm i}$) are free parameters.

Finally, to ensure that the declining density and magnetic field profiles do not fall below observational limits, we add floor values $\rho_{\rm floor} \sim 10^{-6}\rho_{\rm i}$ and $B_{z,{\rm floor}} \sim 10^{-5}B_{\rm i}$ (cf. Bergin & Tafalla 2007; Vallée 2003) to Equations (4) and (5). By imposing HSE and the adiabatic gas law at $t = 0$, a floor value on ρ imposes effective floor values on $\vec{g}$ and p as well.

2.2. Boundary Conditions

In the accretion disk ($z \leqslant 0$, $r \geqslant r_{\rm i}$), $v_{\varphi} = v_{\rm K} = \sqrt{GM_*/r}$, the Keplerian speed, and $v_z = \zeta v_{\rm K} = 10^{-3}v_{\rm K}$ is an "evaporation speed" at the disk surface. The disk and atmosphere are initially

in pressure balance with a density contrast $\eta = \rho_{\rm disc}/\rho_{\rm atm} = 100$, while $\vec{B}$ is initialized using Equations (5).

Following Krasnopolsky et al. (1999), ρ, p, and v_z are held constant, $v_r = v_z B_r/B_z$, $v_{\varphi} = v_{\rm K} + v_z B_{\varphi}/B_z$, $E_z(-z) = E_z(z)$ (where $\vec{E} = \vec{v}\times\vec{B}$ is the induced electric field), $E_r(0) = v_{\rm K}B_z(0)$, $E_r(-z) = E_r(0) - E_r(z)$, $E_{\varphi}(0) = 0$, and $E_{\varphi}(-z) = -E_{\varphi}(z)$. Since v_z is subslow, these conditions are formally overdetermined and p should probably be allowed to float. Indeed, we allowed p to be determined self-consistently in test simulations and found only minor quantitative differences in the jet since the pressure gradient is only about 1% of the net Lorentz force at the disk surface. However, allowing p to float in the boundary caused undue high temperatures in the disk, and thus small time steps. Therefore, the simulation proceeds more rapidly but otherwise virtually unchanged when p is maintained at its initial value.

Inside $r_{\rm i}$ ($z \leqslant 0$), we apply reflecting, conducting boundary conditions ($\vec{J} = \nabla\times\vec{B} \neq 0$). Thus, ρ, p, and $\vec{v}$ are reflected across $z = 0$, and magnetic boundary conditions are set according to $E_z(-z) = -E_z(z)$, $E_r(-z) = E_r(z)$, and $E_{\varphi}(-z) = E_{\varphi}(z)$. At $z = 0$, E_r and E_{φ} are evolved using the full MHD equations.

Finally, we use reflecting boundary conditions along the $r = 0$ symmetry axis, and outflow conditions along the outermost r and z boundaries. Since nothing reaches these outermost boundaries, the nature of the outflow conditions is moot.

2.3. Scaling Relations

From Equation (1) and the adiabatic gas law, one can show

$$c_{\rm s}^2 = \gamma\frac{p}{\rho} = (\gamma-1)\frac{GM_*}{R} = (\gamma-1)v_{\rm K}^2, \qquad (7)$$

where R is the spherical polar radius. From Equations (6) and (7), and the ideal gas law ($p = \rho kT/\langle m\rangle$, where $\langle m\rangle$ is half a proton mass), we derive the following scaling relations:

$$p_{\rm i} = (160\ {\rm dyne\ cm}^{-2})\left(\frac{\beta_{\rm i}}{40}\right)\left(\frac{B_{\rm i}}{10\ {\rm G}}\right)^2; \qquad (8)$$

$$\frac{\rho_{\rm i}}{\langle m\rangle} = (5.4\times10^{12}\ {\rm cm}^{-3})\left(\frac{\beta_{\rm i}}{40}\right)\left(\frac{B_{\rm i}}{10\ {\rm G}}\right)^2\left(\frac{r_{\rm i}}{0.05\ {\rm AU}}\right)$$
$$\times\left(\frac{0.5\ M_{\odot}}{M_*}\right); \qquad (9)$$

$$T_{\rm i} = (2.2\times10^5\ {\rm K})\left(\frac{0.05\ {\rm AU}}{r_{\rm i}}\right)\left(\frac{M_*}{0.5\ M_{\odot}}\right); \qquad (10)$$

$$c_{\rm s,i} = (77\ {\rm km\ s}^{-1})\left(\frac{0.05\ {\rm AU}}{r_{\rm i}}\right)^{1/2}\left(\frac{M_*}{0.5\ M_{\odot}}\right)^{1/2}; \qquad (11)$$

$$\tau_{\rm i} = \frac{r_{\rm i}}{c_{\rm s,i}} = (9.7\times10^4\ {\rm s})\left(\frac{r_{\rm i}}{0.05\ {\rm AU}}\right)^{3/2}\left(\frac{0.5\ M_{\odot}}{M_*}\right)^{1/2}, \qquad (12)$$

for $\gamma = 5/3$. Note that $\beta_{\rm i}$ is the only free parameter varied in this work.

3. RESULTS FOR $\beta_{\rm i} = 40$

Figure 1 depicts a jet with $\beta_{\rm i} = 40$ at $t \simeq 100$ yr from the highest resolution grid near the disk surface (bottom panel) to the coarsest grid in which the jet has reached a length of
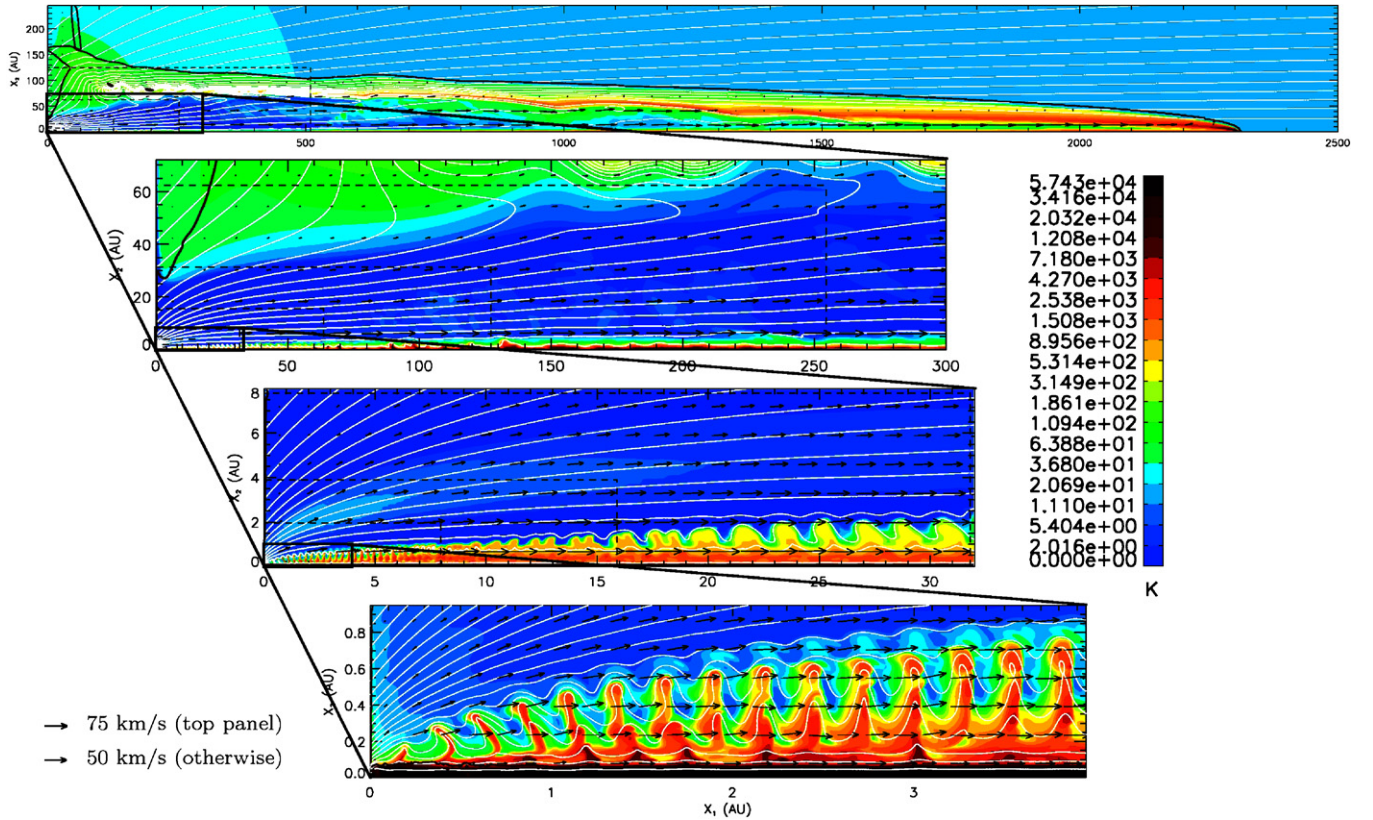
Figure 1. Nested images of a $\beta_i = 40$ jet at $t = 100$ yr. Colors indicate temperature, white contours magnetic field lines, maroon contours the slow surface, and arrows the velocity. Dashed lines denote grid boundaries.

just under 2500 AU (top panel).[3] A few features worth noting include the following.

1. When $\theta < 60°$ (angle between $\vec{B}_p$ and disk surface), Blandford & Payne ([1982](#)) show that cold gas near the disk is launched into a collimated outflow. Here, $\theta < 60°$ for all $r > r_i$, but significant outflow is limited to inside the point where the slow surface intersects the disk ($r_{j,d} \sim 30$ AU = jet radius at the disk; the second panel from top). Below $r_{j,d}$, cold disk material has moved onto the grid and accelerated into the outflow. Above $r_{j,d}$, the weak magnetic field has yet to drive enough disk material onto the grid to displace the hot atmosphere, and outflow is stifled. While $r_{j,d}$ gradually increases with time, the majority of mass flux originating from the disk is driven within $r_i < r < 10\,r_i$ (0.5 AU; bottom panel).

2. Jet material becomes superfast ($M_f \lesssim 5$) within a few AU of the disk, and the boundary between jet and entrained ambient material is defined by a steep temperature gradient (contact discontinuity; second panel). Portions of the original atmosphere, which remain virtually stationary throughout the simulation, are still visible above and ahead of the bow shock (top panel).

3. At large distances from the disk ($\gtrsim 500$ AU; top panel), the dynamics of the jet become dominated by B_φ, and the jet is led by an essentially ballistic, magnetic "nose-cone" with a Mach number of ~ 10 (e.g., Clarke et al. [1986](#)). Still, B_φ is a small fraction (10^{-3}) of B_i, consistent with Hartigan et al. ([2007](#)).

4. The knots dominating the bottom panel (cf., Ouyed & Pudritz [1997b](#)) are produced by the nearly harmonic oscillation of $\vec{B}_p$ in $r_i < r < 2\,r_i$, whereby θ fluctuates between 55° and 65° with a period $\sim 30\,\tau_i$. These oscillations result from the interplay between infalling material along the symmetry axis, and under/over pressurisation near the central mass. The knots are denser and hotter than their surroundings, and bound by magnetic field loops. They occupy a region within ~ 2 AU of the symmetry axis and gradually merge to form a continuous and narrow column of hot, magnetized material[4] (third panel). As such, they are unlikely to be the origin of the much larger-scale knots observed in some jets (e.g., HH111; Raga et al. [2002](#)).

Further details of this and other simulations of protostellar jets are left to a future paper, and we focus here on a few properties directly comparable with observations.

4. COMPARING SIMULATIONS AND OBSERVATIONS

Table [1](#) summarizes a few observational characteristics of protostellar jets. To connect these attributes to conditions in the launching region, we have performed a small parameter survey in β_i and made numerical measurements of the quantities in Table [1](#). Variation of other parameters (such as ζ and ρ_i) is left to future work.

Note that β_i is the initial value of the plasma beta at r_i, and not the average β in the jet. Indeed, Figure [2](#)(a) demonstrates that at very early time, $\langle\beta\rangle = 8\pi\langle p\rangle/\langle B^2\rangle \lesssim \beta_i/5$, where $B^2 = B_p^2 + B_\varphi^2$, and where the average is taken over zones

---

[3] Time-lapse animations are available at http://www.ica.smu.ca/zeus3d/rc10/.

[4] The knots are resolved by 10–20 zones when they merge, and thus their merger is unlikely related to the ever-decreasing resolution of the nested grids.
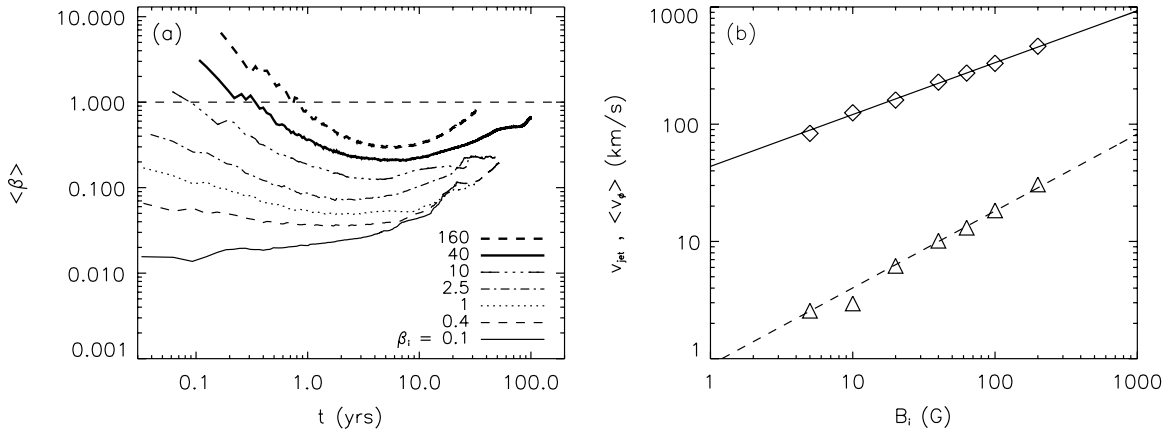
Figure 2. (a) $\langle\beta\rangle$ as a function of time for different β_i. (b) v_{jet} (diamonds) and $\langle v_\varphi\rangle$ (triangles) of each jet as a function of B_i. Best-fit power-law coefficients for these data are $\alpha = 0.44 \pm 0.01$ (v_{jet}, solid line) and 0.66 ± 0.01 ($\langle v_\varphi\rangle$, dashed line).

Table 1
Selected Observational Characteristics of Protostellar Jets

Proper motion (km s^{-1})	100–200 (500 max.)
Rotational velocity (km s^{-1})	(5–25) $\pm$ 5
FWHM jet width (AU)	30–80 (at 200 AU)
Mass-loss rate ($10^{-6} M_\odot$ yr^{-1})	0.01–1

References. Reipurth & Bally 2001; Ray et al. 2007; McKee & Ostriker 2007.

that exceed a certain threshold v_z so that only outflowing jet material is considered. Thus, the magnetic field within the jet is stronger than β_i would suggest. Initially, $\langle\beta\rangle$ is dictated by B_p, but becomes dominated by B_φ within $\lesssim 10$ yr after launch. As time progresses, $\langle\beta\rangle$ gradually increases but never rises above unity (at least for $t < 100$ yr), even for $\beta_i \gg 1$. Still, one might speculate from Figure 2(a) that with sufficient time, $\langle\beta\rangle \to 1$ regardless of β_i.

4.1. Proper Motion

For $t \gtrsim 10$ yr, the velocity of the tip of the jet, v_{jet}, attains a steady value and, from Figure 2(b) and Table 2, we find $v_{jet} \propto B_i^{0.44 \pm 0.01}$.

To understand this result physically, we begin with the magnetic forces:

$$F_\parallel = -\frac{B_\varphi}{r}\nabla_\parallel(r B_\varphi);$$
$$F_\varphi = \frac{B_p}{r}\nabla_\parallel(r B_\varphi); \qquad (13)$$
$$F_\perp = -\frac{B_\varphi}{r}\nabla_\perp(r B_\varphi) + J_\varphi B_p$$

(e.g., Ferreira 1997; Zanni et al. 2007), where $\nabla_\parallel$ and $\nabla_\perp$ are the gradients parallel and perpendicular to $\vec{B}_p$, respectively. For a given field line, a stronger B_p at its "footprint" in the disk ($r = r_0$) generates a stronger B_φ which leads to stronger gradients in $r B_\varphi$ and thus, from Equations (13), greater magnetic forces to accelerate the flow. In practice, we find that most of the acceleration occurs before the fast point (and not the Alfvén point) located at $r = r_f$, where r_f is a weak function of the field strength at the footprint and thus of B_i.

Following Spruit (1996), one can show that as a function of the "fast moment arm" ($\xi \equiv r_f/r_0$), the poloidal velocity at the

fast point is

$$v_{p,f} = \sqrt{a_{p,f}\, v_{K,0}}\left(\xi^2 + \frac{2}{\xi} - 3\right)^{1/4} \propto \sqrt{B_i}, \qquad (14)$$

since $a_{p,f}$, the poloidal Alfvén speed at the fast point, is roughly proportional to B_i. $v_{K,0} = \sqrt{GM_*/r_0}$ is the Keplerian speed at the footprint of the field line. We note that measured values of $v_{p,f}$ in our simulations vary as $B_i^{0.5}$ and agree with Equation (14) to within 1% so long as the fluid is in approximate steady state.[5]

After the poloidal force given by Equations (13) decreases to 1% of its maximum value ($\gtrsim$ a few r_f), v_p still follows a power law in B_i with index 0.52 ± 0.04 and essentially unchanged from Equation (14). Nearer the head of the jet where steady state is no longer valid, we find $\langle v_p\rangle \propto B_i^{0.45 \pm 0.02}$ (where the momentum-weighted average is taken across the jet radius), only slightly shallower than Equation (14). Thus, while the conditions in the jet have changed, some memory of the steady-state conditions at r_f persists.

Finally, v_{jet} (Figure 2(b) and Table 2) is within $\sim$10% of $\langle v_p\rangle$ near the bow shock and maintains the same power-law dependence on B_i. Thus, these jets are essentially ballistic, where the observed jet speed $v_{jet} \propto B_i^{0.44 \pm 0.01}$. In short, all measures of jet speed increase with B_i, a trend that agrees with Anderson et al. (2005) who find for much less evolved jets, $v_p \propto B_i^{1/3}$.

4.2. Toroidal Velocity

Figure 2(b) and Table 2 show v_φ averaged over time and the jet volume for $z \geqslant 100$ AU as a function of B_i. Like v_{jet}, v_φ asymptotes to a constant value. The region inside 100 AU is ignored because the torsion Alfvén wave at low z has a non-negligible v_φ, is not part of the jet, and skews our results. By fitting a power law to these data, we find $\langle v_\varphi\rangle \propto B_i^{0.66 \pm 0.01}$.

Unlike v_{jet}, we have not uncovered a rationale for this power law, yet it seems plausible that one must exist given the tightness of fit. Eliminating B_i from the power laws for $\langle v_\varphi\rangle$ and v_{jet}, we find that $\langle v_\varphi\rangle \propto v_{jet}^{1.50 \pm 0.04}$. To render this a useful observational tool, further work is needed to quantify the effects of other initial conditions such as ζ and ρ_i on both the power-law index and the proportionality constant, as well as the effect our simplified

---

[5] Indeed, all four steady-state functions from Spruit (1996) remain constant in our simulations to within $\lesssim$5% along steady-state field lines, which we take as validation of our numerical methods.

Table 2
Simulation "Observables" $v_{\rm jet}$ and $\langle v_\varphi \rangle$ are Asymptotic Values While $r_{\rm jet}$ and $\dot{M}_{\rm jet}$ are Measured at $z = 200$ AU and $t = 20$ yr

$\beta_{\rm i}$	160	40	10	2.5	1.0	0.4	0.1	α
$B_{\rm i}$ (G)	5	10	20	40	63.2	100	200	
$v_{\rm jet}$ (km s^{-1})	84	125	161	230	270	330	460	0.44 ± 0.01
$\langle v_\varphi \rangle$ (km s^{-1})	2.6	3.0	6.2	10.1	13.1	18.4	31	0.66 ± 0.01
$2\,r_{\rm jet}$ (AU)	21	40	60	85	94	104	130	0.35 ± 0.04
$\dot{M}_{\rm jet}$ ($10^{-6}\,M_\odot$ yr^{-1})	0.44	1.9	2.8	4.2	6.9	10.1	17.9	0.92 ± 0.09

Note. Uncertainties in α are from the fitting procedure.

disk model may have on conditions in the jet at observational length scales.

4.3. Jet Radius and Mass Flux

The jet radius, $r_{\rm jet}$, is defined by the contact discontinuity (steep temperature gradient in the second panel of Figure 1) between shocked jet and shocked ambient material, which in turn is determined by where the radial jet ram pressure balances all external forces. Since ram pressure increases with $v_{\rm p}$, $r_{\rm jet}$ should increase with $B_{\rm i}$, just as observed in Table 2. At any given time, we find that $r_{\rm jet}$ varies with $B_{\rm i}$ as a reasonable power law though, unlike $v_{\rm jet}$ or $\langle v_\varphi \rangle$, the power index is not constant and decreases slowly in time, while $r_{\rm jet}$ itself increases in time, though at an ever-slowing rate.

The mass flux transported by the jet, $\dot{M}_{\rm jet}$, consists of material from both the disk and the atmosphere. Unlike previous simulations where jets are typically evolved long after the leading bow shock has left the grid, no part of any bow shock in our simulations reaches the boundary of the coarsest grid. Thus, each jet continues to entrain material from the atmosphere throughout the simulation at a rate that has a strong dependence on $B_{\rm i}$, as seen in Table 2. Indeed we find that $\dot{M}_{\rm jet}$ varies with $B_{\rm i}$ as a reasonable power law, with the power index decreasing slowly in time. As the atmosphere is depleted, the mass flux contribution from the disk (which, by design, is independent of $B_{\rm i}$) becomes more important and the dependence of $\dot{M}_{\rm jet}$ on $B_{\rm i}$ diminishes.

5. DISCUSSION

We have presented the first MHD simulations of protostellar jets that start from a well-resolved launching region ($\Delta z_{\rm min} = 0.00625$ AU) and continue well into the observational domain (2500 AU). On the AU scale, each jet shows the characteristic and near steady-state knotty behavior first reported by Ouyed & Pudritz (1997b), though the origin of our knots is quite different. On the 1000 AU scale, each jet develops into a ballistic, supersonic ($8 \lesssim M \lesssim 11$) outflow led by a magnetically confined "nose-cone" (Clarke et al. 1986) and a narrow bow shock, consistent with what is normally observed.

On comparing Tables 1 and 2, our simulations comfortably contain virtually all observed protostellar jets on these four important quantities. We note that these tables would *not* have been in agreement had we stopped the jet at, say, 100 AU and measured these values then. *It is only because our jets have evolved over five orders of magnitude in length scale that we can state with some confidence that the magnetocentrifugal launching mechanism is, by itself, capable of producing jets with the observed proper motion, rotational velocity, radius, and mass outflow rate.* Indeed, our jets are still very young, having evolved to only 100 yr, and allowing them to evolve over an additional one or two orders of magnitude in time may still

be useful. For example, it would be interesting to know whether $\langle \beta \rangle$ rises above unity for any of the jets (Figure 2(a)), and thus enter into a hydrodynamically dominated regime. It would also be interesting to see how long it takes for the power laws in jet radius and mass flux as a function of $B_{\rm i}$ to reach their asymptotic limits.

Our jet widths tend to be higher than those observed, particularly when one considers that the values for $r_{\rm jet}$ in Table 2 are at $t = 20$ yr,[6] and that $r_{\rm jet}$ continues to grow in time (e.g., for the $\beta_{\rm i} = 40$ jet, $2\,r_{\rm jet} \sim 100$ AU by $t = 100$ yr). As our jet radii mark the locations of the contact discontinuity while observed radii mark hot, emitting regions, our widths should be considered upper limits. That our values contain all observed jet widths is a success of these simulations.

Similarly, our numerical mass fluxes are higher than observed values by at least an order of magnitude. Since observed mass-loss rates account only for emitting material (e.g., in forbidden lines; Hartigan et al. 1994), and thus temperatures in excess of 10^4 K (Dyson & Williams 1997, p. 104), our mass fluxes are necessarily upper limits as well. Indeed, if we measure our mass fluxes near the jet tip (instead of at 200 AU for Table 2) and restrict the integration to fluid above 10^4 K, our mass fluxes drop by a factor of 10–100, in much better agreement with Table 1.

REFERENCES

Anderson, J. M., Li, Z.-Y., Krasnopolsky, R., & Blandford, R. D. 2005, ApJ, 630, 945
Bally, J., Reipurth, B., & Davis, C. J. 2007, in Protostars and Planets V, ed. B. Reipurth, D. Jewitt, & K. Keil (Tucson, AZ: Univ. Arizona Press), 215
Bell, J., Berger, M., Saltzman, J., & Welcome, M. 1994, SIAM J. Sci. Comput., 15, 127
Berger, M. J., & Colella, P. 1989, J. Comput. Phys., 82, 64
Bergin, E. A., & Tafalla, M. 2007, ARA&A, 45, 339
Blandford, R. D., & Payne, D. G. 1982, MNRAS, 199, 883
Calvet, N., Hartmann, L., & Strom, S. E. 2000, in Protostars and Planets IV, ed. V. Mannings, A. P. Boss, & S. S. Russell (Tucson, AZ: Univ. Arizona Press), 377
Clarke, D. A. 1996, ApJ, 457, 291
Clarke, D. A. 2010, ApJS, 187, 119
Clarke, D. A., Norman, M. L., & Burns, J. O. 1986, ApJ, 311, L63
Coffey, D., Bacciotti, F., & Podio, L. 2008, ApJ, 689, 1112

---

[6] Some simulations had not reached $t = 100$ yr at the time of this writing.

Dyson, J. E., & Williams, D. A. (ed.) 1997, The Physics of the Interstellar Medium (2nd ed.; Bristol: IOP Publishing)
Ferreira, J. 1997, A&A, 319, 340
Hartigan, P., Edwards, S., & Pierson, R. 2004, ApJ, 609, 261
Hartigan, P., Frank, A., Varniére, P., & Blackman, E. G. 2007, ApJ, 661, 910
Hartigan, P., Morse, J. A., & Raymond, J. 1994, ApJ, 436, 125
Krasnopolsky, R., Li, Z.-Y., & Blandford, R. 1999, ApJ, 526, 631
McKee, C. F., & Ostriker, E. C. 2007, ARA&A, 45, 565
Meier, D. L., Edgington, S., Godon, P., Payne, D. G., & Lind, K. R. 1997, Nature, 388, 350
O'Shea, B. W., Bryan, G., Bordner, J., Norman, M. L., Abel, T., Harkness, R., & Kritsuk, A. 2004, arXiv:astro-ph/0403044
Ouyed, R., Clarke, D. A., & Pudritz, R. E. 2003, ApJ, 582, 292
Ouyed, R., & Pudritz, R. E. 1997a, ApJ, 482, 712
Ouyed, R., & Pudritz, R. E. 1997b, ApJ, 484, 794
Ouyed, R., & Pudritz, R. E. 1999, MNRAS, 309, 233
Porth, O., & Fendt, C. 2010, ApJ, 709, 1100
Pudritz, R. E., Ouyed, R., Fendt, C., & Brandenburg, A. 2007, in Protostars and Planets V, ed. B. Reipurth, D. Jewitt, & K. Keil (Tucson, AZ: Univ. Arizona Press), 277
Raga, A. C., Noriega-Crespo, A., Reipurth, B., Garnavich, P. M., Heathcote, S., Böhm, K. H., & Curiel, S. 2002, ApJ, 565, L29
Ray, T., Dougados, C., Bacciotti, F., Eislöffel, J., & Chrysostomou, A. 2007, in Protostars and Planets V, ed. B. Reipurth, D. Jewitt, & K. Keil (Tucson, AZ: Univ. Arizona Press), 231
Reipurth, B., & Bally, J. 2001, ARA&A, 39, 403
Spruit, H. C. 1996, in Phys Processes in Binary Stars, ed. R. A. M. J. Wijers, M. B. Davies, & C. A. Tout (Dordrecht: Kluwer), 249
Staff, J. E., Niebergal, B. P., Ouyed, R., Pudritz, R. E., & Cai, K. 2010, ApJ, 722, 1325
Uchida, Y., & Shibata, K. 1985, PASJ, 37, 515
Ustyugova, G. V., Kolboda, A. V., Romanova, M. M., Chechetkin, V. M., & Lovelace, R. V. E. 1995, ApJ, 439, 3
Vallée, J. P. 2003, New Astron. Rev., 47, 85
Vitorino, B. F., Jatenco-Pereira, V., & Opher, R. 2002, A&A, 384, 329
von Rekowski, B., Brandenburg, A., Dobler, W., & Shukurov, A. 2003, A&A, 398, 825
Zanni, C., Ferrari, A., Rosner, R., Bodo, G., & Massaglia, S. 2007, A&A, 469, 811